



# The influence of surface heat fluxes on the growth of idealized monsoon

## depressions

Michael Diaz\*

*Department of Earth and Planetary Science, University of California, Berkeley, USA*

William R. Boos

*Department of Earth and Planetary Science, University of California, Berkeley, USA*

*Climate and Ecosystem Sciences Division, Lawrence Berkeley National Laboratory, Berkeley, California, USA*

\*Corresponding author: Michael Diaz, mldiaz@ncsu.edu

## ABSTRACT

This study explores the effect of surface sensible and latent heat fluxes on monsoon depressions using a series of idealized convection-permitting simulations. Each experiment is initialized with a small amplitude wave that is allowed to grow within an environment representative of the South Asian monsoon. Comparing experiments with and without interactive surface heat fluxes, it is found that these fluxes enhance the growth of the simulated vortices. Without interactive surface fluxes, the strengthening period is short and the vortices fail to reach intensities characteristic of stronger monsoon depressions. Using a large set of experiments in which the vertical and meridional shear are systematically varied, it is found that surface heat fluxes enhance intensity the most when the upper-level shear is weak, the lower-level shear and associated moist static energy (MSE) gradient are sufficiently steep, and the lower-level meridional shear is strong. These experiments reveal two different regimes of convection-coupled monsoon depression growth: one in which convection is driven by MSE advection and one in which it is driven by surface heat fluxes and quasi-geostrophic forcing for ascent. Both regimes require sufficiently strong meridional shear to achieve initial growth by barotropic instability.

## 1. Introduction

The Bay of Bengal exhibits a seasonal cycle of tropical cyclone activity that is unique among the world's ocean basins: cyclone frequency peaks sharply in both May and November, with a relative minimum during boreal summer. This minimum is brought about by the South Asian monsoon, whose increased vertical wind shear inhibits tropical cyclogenesis, despite favorably high relative humidity and sea surface temperatures (Tippett et al. 2011). During the monsoon, however, another class of synoptic-scale weather systems forms: the monsoon depression. Although it is well established that surface sensible and latent heat fluxes are essential for tropical cyclone growth (Rotunno and Emanuel 1987), it is less clear to what extent they impact monsoon depressions. Considering that they resemble weak tropical cyclones and that a number of other weather systems can amplify through heat exchanges with the ocean, including mid-latitude cyclones (Uccellini 1990), polar lows (Emanuel and Rotunno 1989), and subtropical cyclones, it is reasonable to expect that surface heat fluxes might also be important for monsoon depressions.

A few recent studies have shed light on the role of surface heat fluxes in the development of monsoon depressions. One of the more relevant is Fujinami et al. (2020), which compares two simulations of an observed monsoon depression: one with fully interactive surface heat fluxes and one without any surface heat fluxes. They argue that these fluxes are essential for its rapid intensification, because they provide a moisture source to fuel the convection. Diaz and Boos (2019b) performed a similar experiment with an idealized monsoon depression, but with somewhat different results. Although including interactive surface heat fluxes led to a somewhat stronger storm, setting the surface heat fluxes to be independent of perturbation winds, temperatures, and humidities did not prevent its rapid intensification. Murthy and Boos (2020) took an even more idealized approach of using a column Quasi-Geostrophic (QG) model with large-

scale temperature, vorticity, and moisture advection set to mimic the convectively active region of a monsoon depression. They found that surface fluxes contributed to 40% of the increase in precipitation relative to a resting state in radiative-convective equilibrium. Additionally, although not emphasized in their study, Clark et al. (2020) found that surface fluxes contributed substantially to maintaining the moist static energy (MSE) of monsoon depression-like disturbances in an idealized General Circulation Model (GCM). By contrast, in another idealized GCM study, Adames and Ming (2018b) found that the contribution of surface fluxes to maintaining MSE was minimal. Other studies have looked at surface fluxes over land and found that soil moisture anomalies allowed monsoon depressions to penetrate farther inland by enhancing surface latent heat fluxes (Kishtawal et al. 2013; Hunt and Turner 2017).

Regardless of the role of surface fluxes, most studies that attempt to isolate the fundamental growth mechanism of monsoon depressions highlight other processes as more important. Several recent studies have hypothesized the interaction of the rotational winds of the depression with the climatological poleward MSE gradient to be essential for their growth (Adames and Ming 2018b,a; Clark et al. 2020). According to this hypothesis, positive MSE advection to the west of the circulation center generates convection. Vortex stretching induced by this convection then leads to amplification of the larger-scale monsoon depression circulation. By contrast, Diaz and Boos (2019b) argues that monsoon depressions are a type of moist barotropic instability that grows by drawing energy from both the meridional shear of the monsoon trough and from coupling with moist convection. This convection is coupled to the vortex by the interaction of the vortex's rotational wind with the background vertical shear, which leads to QG forcing for ascent.

In a companion paper to the current study, Diaz and Boos (2021) (DB2021) performed a large suite of idealized simulations of monsoon depression-like vortices with varying amounts of basic state meridional and vertical wind shear, but without surface heat fluxes that interact with the

winds and thermodynamic state of the vortices. Through the constraints of thermal wind balance and constant relative humidity, these variations in the basic state shears also control the MSE gradient by setting the basic state meridional gradients of temperature and moisture. Based on their results, DB2021 highlighted two factors that could be important for monsoon depression growth: a sufficiently strong low-level MSE gradient and adequate meridional wind shear. The vortices in these experiments undergo a life cycle whereby they intensify through both barotropic instability and through their interaction with moist convection, with the strength of this convection being a strong function of the basic state MSE gradient. This finding lends partial support to hypotheses of Adames and Ming (2018b) and Diaz and Boos (2019b). However, amplification through these processes was brief and resulted in only modest growth, with peak intensities not reaching those of stronger monsoon depressions observed in the real atmosphere. One possibility for this limited growth is the absence of surface heat fluxes. The goal of the present study is to test this idea by employing the same suite of experiments used in DB2021. We will also examine surface heat fluxes in monsoon depressions in reanalysis data.

## 2. Observed Surface Fluxes

To inform the experimental design and subsequent analysis, it is useful to examine surface heat fluxes and vertical wind shear in observed monsoon depressions. For this purpose, we use the ERA5 reanalysis (Hersbach et al. 2020) to create a storm-centered composite using monsoon depression track data from the India Meteorological Department (IMD) from 1982 to 2018. Since the behavior of surface heat fluxes differs dramatically between land and ocean, and because our subsequent experiments will implement fluxes characteristic of an ocean, we limit the composite to times when each monsoon depression was over the Bay of Bengal. To calculate anomalies from the mean state, we build a storm-centered climatology by averaging the same hour for every other

year while maintaining the center of the composite coincident with the center of the storm. For example, if a storm occurs on 1 July 2018 at 12 UTC centered at  $19^{\circ}N$ ,  $88^{\circ}E$ , the climatology would include 36 frames from the years 1982 to 2017 at 1 July 12 UTC. The resulting composite is shown in Fig. 1, with the map positioned according to the mean latitude and longitude of the composite.

The composite monsoon depression is centered in the northern Bay of Bengal (Fig. 1). Consistent with many previous studies (e.g. Boos et al. 2015; Hunt et al. 2016), the anomalous rainfall is biased toward the southwestern quadrant and its circulation is embedded within substantial easterly vertical wind shear (Fig. 1a). This shear varies strongly with latitude, with magnitudes exceeding  $30\text{ m s}^{-1}$  to the south and approaching  $0\text{ m s}^{-1}$  to the north. The circulation center is embedded within this strong gradient of vertical shear. While this distribution partly results from the cyclonic circulation of the monsoon depression, the strong shear gradient is also a robust feature of the background climatology (figure 2 in Diaz and Boos (2019a) and figure 2 in Boos et al. (2015)). The anomalous surface latent and sensible heat fluxes are shown in Fig. 1b. The largest latent heat fluxes are located south of the circulation center within the strong westerly flow. Although the near-surface anomalous wind is not particularly strong in this region relative to the rest of the circulation, the flux is stronger because the climatological westerly flow present throughout the Bay of Bengal adds constructively to the perturbation flow. The maximum in sensible heat flux is also located south of the circulation center, though it is about an order of magnitude weaker. Over most of the land area, the latent heat flux is near zero. The sensible heat flux, by contrast, exhibits a significant negative anomaly over land. This feature is presumably caused by increased cloud cover and rain blocking surface insolation. One should however exercise a bit of caution when interpreting geographic aspects of this plot, since it is storm centered and hence contains a mixture of land and ocean points in the vicinity of where the coastlines are drawn. Nevertheless, the monsoon depressions in this

composite are so tightly clustered in the northern Bay of Bengal that the overlap between land and water points between averaging frames is very small.

### 3. Experimental Design

The design of this study is essentially the same as that of DB2021, but with the addition of interactive surface sensible and latent heat fluxes. DB2021 used a numerical model that separates the atmosphere into a basic state and a perturbation in order to investigate how the background environment affects monsoon depression-like vortices (for details of the model, see Diaz and Boos (2019a)). Basic states were created with varying amounts of horizontal and vertical wind shear in order to replicate a wide range of monsoonal environments characteristic of South Asia. Within each basic state, a small amplitude disturbance was initialized and its subsequent evolution examined. Further details of the model equations and physics can be found in DB2021.

Although previous studies also examined how surface heat fluxes influence monsoon depressions, our experimental design offers a few advantages. In contrast with Diaz and Boos (2019b), who used a single complicated basic state from a reanalysis dataset, we examine a multitude of simpler basic states with a variety of shear profiles. Considering how sensitive tropical cyclones are to vertical shear, it is reasonable to expect that surface heat fluxes affect monsoon depressions differently depending on the magnitude of shear. Additionally, our model equations allow us to alter only the perturbation surface heat flux, rather than the full flux, as in Fujinami et al. (2020). Such a feature allows for a more controlled experiment. Finally, in contrast with Clark et al. (2020) and Adames and Ming (2018b), whose coarser resolution required using a convective parameterization, we use convection-permitting simulations.

### a. Basic States

The procedure to construct the basic state is identical to that of DB2021. All basic states are expressed as the sum of two zonally uniform components: a profile of zonal wind that varies only in height and a monsoon trough-like feature with enhanced meridional shear concentrated near the surface. The temperature and moisture fields are derived based on realistic balance constraints.

The first component of the basic state is defined in terms of its vertical shear as

$$\frac{\partial \bar{U}}{\partial z}(z) = \begin{cases} S_L + z \frac{S_U - S_L}{h_U - h_L} & z \leq h_U \\ S_U & z > h_U \end{cases} \quad (1a)$$

$$S_L \equiv \partial_z \bar{U}(h_L) \quad (1b)$$

$$S_U \equiv \partial_z \bar{U}(h_U) \quad (1c)$$

$$\bar{U}(h_0) = 3 \text{ m s}^{-1} \quad (1d)$$

where  $h_L = 0 \text{ km}$ ,  $h_U = 16.6 \text{ km}$ , and  $h_0 = 4.0 \text{ km}$ . This functional form allows us to concentrate the vertical shear in either the lower ( $S_L$ ) or upper ( $S_U$ ) troposphere, resulting in vertical profiles of  $\bar{U}$  that are parabolic. To create the meridional distribution of  $\bar{U}$ , we begin with a distribution of relative vorticity, given by

$$\begin{aligned} \zeta(y, z) = \zeta_0 & \left[ \cos \left( -\pi + 2\pi \frac{y - y_0}{y_1 - y_0} \right) + 1 \right] \times \\ & \left[ \cos \left( -0.1\pi + 1.2\pi \frac{z - z_0}{z_1 - z_0} \right) + 1 \right] \end{aligned} \quad (2)$$

defined on the interval  $y_0$  to  $y_1$  where  $y_0 = 18^\circ N$ ,  $y_1 = 21^\circ N$ ,  $z_0 = 0 \text{ m}$ , and  $z_1 = 17.0 \text{ km}$ . The wind field is then obtained by solving

$$\frac{\partial^2 \bar{U}}{\partial y^2} = \zeta(y, z) \quad (3)$$

with periodic lateral boundaries in the zonal direction and zero-gradient boundaries in the north and south. The final basic state zonal wind field is constructed by adding  $\bar{U}$  from Eq. 1 and  $\bar{U}$

from Eq. 3. This procedure leaves us with three tunable parameters for the basic state, namely  $S_L$ ,  $S_U$ , and  $\zeta_0$ , which control the lower-level vertical shear, upper-level vertical shear, and lower-level meridional shear, respectively. The temperature field is set using thermal wind balance and the moisture field using constant relative humidity within the latitude band of interest with decreasing values outside of this region. Details on how the temperature and moisture fields are constructed are given in DB2021, as well as cross sections for all basic state variables for every combination of parameters used in this study.

To demonstrate how these parameters affect vertical wind shear, we examine how the vertical shear of the zonal wind changes as one parameter varies while the other two are held constant for various combinations used in our experiments (Fig. 2). Figure 2a shows the 850 hPa to 200 hPa vertical shear as a function of latitude for different values of  $\zeta_0$ . This shear metric is chosen because it is commonly employed in studies of tropical cyclones. With its effects being biggest near the surface, increasing  $\zeta_0$  weakens vertical shear to the north and strengthens it to the south, leading to a large meridional gradient in vertical shear along the axis of the monsoon trough near  $20^\circ N$ . As discussed in Sec. 2, this gradient is a realistic feature of the background climatology. This meridionally varying shear makes direct comparisons with previous idealized modeling studies of tropical cyclones somewhat difficult, as they typically use spatially uniform shear. Figures 2b and 2c show zonal shear as a function of height for variations in  $S_U$  and  $S_L$ , respectively. As also seen in Fig. 2a, shear to the south is significantly larger than shear to the north. The bowing in the profiles is caused by  $\zeta(y, z)$ . If  $\zeta_0$  were set to zero, they would be straight lines.

For a rough comparison between these shear profiles and ones typically observed over the Bay of Bengal before the genesis of a monsoon depression, we present profiles of vertical shear of the zonal wind for the pre-genesis composite constructed in Diaz and Boos (2019b) (Fig. 3). This profile is centered at  $21^\circ N$ ,  $90^\circ E$ , near where the simulated vortex in Diaz and Boos (2019b)

strengthened most rapidly. Since our basic state is in thermal wind balance and the meridional temperature gradient is an important feature, we show both the actual zonal wind shear and that calculated based on thermal wind balance. The latter provides a measure of the strength of the meridional temperature gradient in units of wind shear. For comparison, we shade the region of shear covered by the parameter space shown in Fig. 2, but note that this shading does not cover the full range of values used in our experiments.

The vertical profiles of shear for the composite fall mostly within the range covered by the combination of parameters plotted in Fig. 2, with a major exception of within the lowest 1 km (Fig. 2b,c). Here, boundary layer friction slows down the low-level winds, a process that we do not replicate when constructing our idealized basic states. Comparing with individual lines in Fig. 2, it is difficult to assign a single set of parameters to represent the composite profile, as it follows different curves depending on the height and on which side of the monsoon trough axis it lies. Nevertheless, the idealized profiles seem to adequately represent the strong easterly shear and poleward temperature gradient that characterizes the northernmost Bay of Bengal before monsoon depression genesis.

### *b. Surface Fluxes*

The presence of a basic state requires that the surface heat and moisture fluxes be expressed as perturbations. As derived in Diaz and Boos (2019b), the equations for these fluxes are

$$F'_q = C_E \{ -|\mathbf{v}|q' + (|\mathbf{v}| - |\bar{\mathbf{V}}|)(q_s^* - \bar{q} - q_0) \} \quad (4a)$$

$$F'_\theta = C_E \{ -|\mathbf{v}|\theta' + (|\mathbf{v}| - |\bar{\mathbf{V}}|)(T_s - \bar{T}) \} \quad (4b)$$

where  $\mathbf{v}$  and  $\bar{\mathbf{V}}$  are the total and basic state winds at the lowest model level, respectively,  $q'$ ,  $\bar{q}$ , and  $q_0$  are the perturbation, basic state, and base state mixing ratio, respectively,  $q_s^*$  is the saturation

mixing ratio at the ocean surface,  $T_s$  the surface temperature of the ocean, and  $\bar{T}$  the basic state air temperature at the surface. As discussed in DB2021, the *base* state varies in only the vertical direction, whereas the *basic* state can vary both horizontally and vertically. The base state is given in DB2021 (their figure 1) and uses the vertical profile at  $20^\circ N$ ,  $88^\circ E$  in the climatological composite calculated in Diaz and Boos (2019a). Following Rotunno and Emanuel (1987),  $C_E$  is set to

$$C_E = 1.1 \times 10^{-3} + 4 \times 10^{-5} |\mathbf{v}| \quad (5)$$

For all experiments, we use a sea surface temperature of  $29^\circ C$  in the surface flux parameterization for the entire model domain. This value is consistent with buoy observations plotted in Thangaprakash et al. (2016) (their figure 3a).

The approach of partitioning the surface flux into perturbation and basic state components is particularly well suited for testing its impact on monsoon depressions, because they form in a region of strong climatological westerly flow at the surface. With this formulation, we can turn off the perturbation surface fluxes without affecting the basic state fluxes caused by this westerly flow. This is in contrast with experiments such as those in Fujinami et al. (2020), in which the total flux is turned off. To be clear, the basic state surface fluxes in our model are implicit; it is the atmospheric basic state that is imposed, so basic state surface fluxes do not need to be explicitly imposed to maintain that state. Although these implicit fluxes cannot be directly calculated, we note that the climatological mean surface heat fluxes in the ERA5 climatology presented in Sec. 2 averaged over a box bounded by  $15^\circ N$ - $20^\circ N$ ,  $85^\circ E$ - $94^\circ E$  are  $125.5 \text{ W m}^{-2}$  for latent and  $8.1 \text{ W m}^{-2}$  for sensible.

For all experiments, the underlying surface represents water for the entire domain. Though useful for simplicity, this setup is somewhat unrealistic for observed monsoon depressions, because

they generally make landfall within a few days of forming. Consequently, the vortices in these experiments will generally be exposed to ocean-like surface fluxes for longer than their counterparts in the real atmosphere, potentially allowing for higher intensities than are typically observed. Additionally, although the contrast between the land and sea surface is the primary source of the temperature gradient, the warmer region to the north will nevertheless be located over an ocean surface. This situation is less problematic here in comparison with traditional model setups, because the basic state is held constant rather than requiring a balance between convection and radiation.

#### *c. Initial Perturbation and Model Configuration*

The initial condition and model configuration are identical to that of DB2021. Each simulation is run for six days and uses a grid spacing of  $5\text{ km} \times 5\text{ km}$  with 1035 grid points in the east-west direction, 777 in the north-south, and 43 in the vertical. Although this grid spacing is a little larger than typically used in convection-permitting simulations, we find that the strong organization of convection by synoptic-scale flow seems to allow resolutions coarser than typically used in, for example, simulations of radiative-convective equilibrium. Each simulation is initialized with the most unstable normal-mode structure of zonal wavenumber 2 for our domain (i.e. a wavelength of 2587.5 km) for the parameter set of  $\zeta_0 = 1.0$ ,  $S_L = 0$ , and  $S_U = 0$ . Thus, each experiment will result in two vortices.

## **4. Results**

#### *a. Overall Structure*

Figure 4 shows a sample storm from a region of parameter space that favors strong monsoon depression-like vortices. For ease of comparison, this snapshot uses the same set of parameters

and output time as figure 3 in DB2021. The background map is drawn for scale only and is not indicative of the surface characteristics. The structure seen in Fig. 4 resembles a monsoon depression. The strongest convection is located well to the southwest of the circulation center (Fig. 4b), similar to the composite depression (Fig. 1a). The vortex has a warm-over-cold core structure and tilts downshear with height (Fig. 4a,c). Compared with the corresponding simulation in DB2021, which excluded interactive surface heat fluxes, the warm core is stronger and the cold core is weaker. The stronger warm core implies a more intense vortex, and the weaker cold core suggests that surface heat fluxes warm the lower atmosphere. This vortex has a minimum sea-level pressure of 990.8 hPa, which is lower than the 996.2 hPa in the simulation of DB2021. Thus, the addition of surface heat fluxes for this set of parameters yields a stronger vortex whose structure remains characteristic of a monsoon depression.

### b. Life Cycle and Physical Processes

As a starting point for interpreting our experiments, we examine the life cycle of a single case using time series of several metrics found to be useful in DB2021. We choose a set of parameters ( $\zeta_0 = 1.0$ ,  $S_L = -1.25$ , and  $S_U = -1.0$ ) that yields a strong vortex, but still maintains a structure more representative of a monsoon depression than of a classic tropical cyclone. To determine the impact of various physical processes, we show results for three different experiments: one *with* perturbation surface heat fluxes (FluxOn), one *without* perturbation surface heat fluxes (FluxOff), and one in which latent heat release is deactivated (Dry). Figure 5a shows the minimum pressure and rain rate for these three simulations. For the pressure time series, the value given is the minimum within a  $2^\circ \times 2^\circ$  box centered on the centroid of negative pressure. For the rain rate, the three-hour accumulated totals are averaged within a  $10^\circ \times 10^\circ$  box centered on the vortex and

converted to an hourly rate. Both quantities shown are the average of the two vortices that form from the wavenumber 2 perturbation used to initialize the model.

Throughout most of the first day, the minimum pressure for the three experiments is nearly identical and rainfall is absent (Fig. 5a). Thus, the initial strengthening of the vortex is unrelated to moist convection. During days 2 and 3, the experiments begin to diverge. Though FluxOn and FluxOff follow roughly the same pattern, the former produces increasingly more rainfall and lower pressure relative to the latter. After day 3, the gap between the two widens considerably. Rain rates in FluxOn remain nearly steady, while rain rates in FluxOff gradually approach zero. During this period, FluxOff maintains a perturbation pressure of around  $-5$  hPa whereas FluxOn falls to around  $-15$  hPa.

To help explain these results, we calculate select terms in the vertically integrated perturbation MSE budget and the perturbation kinetic energy (PKE) budget. The perturbation MSE tendency equation for a zonally symmetric basic state can be written as

$$\frac{\partial h'}{\partial t} = -(\bar{\mathbf{V}} + \mathbf{v}') \cdot \nabla_2 h' - v' \frac{\partial \bar{h}}{\partial y} - w' \frac{\partial(\bar{h} + h')}{\partial z} + M'_h + T'_h \quad (6)$$

where  $\nabla_2$  is the two-dimensional (horizontal) gradient operator,  $\bar{\mathbf{V}}$  the two-dimensional basic state wind,  $\mathbf{v}'$  the two-dimensional perturbation wind,  $v'$  the meridional perturbation wind,  $w'$  the vertical perturbation wind,  $M'_h$  the tendency from microphysics,  $T'_h$  the tendency from turbulence and surface fluxes, and  $h'$  and  $\bar{h}$  are the perturbation and basic state MSE, respectively. As discussed in Sec. 1, previous studies have argued that horizontal MSE advection is an important organizer of convection in monsoon depressions. To distill this process into a single metric, we note that meridional MSE advection within the northerly flow to the west of the vortex is the essential source of perturbation MSE for organizing convection. We can quantify this advection by averaging the horizontal advection term within a box drawn from the longitude containing the centroid of

negative perturbation pressure at 1.5 km altitude to  $8^\circ$  west of this line, and from  $8^\circ$  to the north of the centroid's latitude to  $8^\circ$  to its south. This procedure is identical to that of DB2021 and is repeated for all of the terms shown in Fig. 5b.

We also examine two terms in the PKE budget: the pressure work term and the barotropic conversion term associated with meridional shear (Fig. 5c,d). They are calculated as in Diaz and Boos (2019a) and averaged over the full domain of the simulation. For these simulations, the pressure work term provides an estimate of how much kinetic energy the vortex gains from latent heating by convection. We assume that this is the dominant process affecting pressure work, because the environment is not baroclinically unstable and this term turns out to be weakly negative when moisture is excluded. The barotropic conversion term ( $u'v'\partial_y\bar{U}$ ) measures kinetic energy gained from the interaction of the disturbance with the basic state meridional shear and is related to barotropic instability.

We first concentrate on the meridional shear term in the PKE budget (Fig. 5c). It starts near its maximum value and then becomes negative by day 2. This pattern suggests an initial state of barotropic instability that the growing vortex extinguishes as it reduces the basic state meridional shear. As the three simulations are nearly identical during the first three days, this process is insensitive to the presence of moisture and surface heat fluxes. During the second half of the simulation, meridional shear again becomes an energy source, but with modest differences among the three simulations. The disturbance in FluxOn gets more energy from this source than do the other two simulations. This difference probably results from the vortex in FluxOn being much stronger than in the other two experiments.

We next examine select terms in the MSE budget and the pressure work term and relate them to rainfall. During the first day, meridional MSE advection dominates MSE growth, with little to no contribution from surface heat fluxes in FluxOn (Fig. 5b). Despite increasing MSE during

this time, there is no rainfall (Fig. 5a) and hence no PKE growth from pressure work (Fig. 5d). Thus, the initial PKE growth comes almost exclusively from barotropic instability (Fig. 5c). The situation changes substantially on day 2; rain rates quickly increase (Fig. 5a) and coupling with moist convection becomes the more significant energy source (Fig. 5d). During day 2 and 3, MSE advection becomes an MSE sink in both moist simulations, while the contribution to MSE from surface fluxes becomes substantial in FluxOn. With the MSE advection term being roughly equal for FluxOn and FluxOff, the addition of perturbation surface heat fluxes in FluxOn causes the values of perturbation MSE for these two simulations to drift apart (Fig. 5b). As time progresses, MSE in FluxOff gradually decreases and becomes negative, while MSE in FluxOn holds steady and eventually begins to increase once again. Consequently, the vortex in FluxOn maintains high rain rates and thus continues to intensify through pressure work, whereas the one in FluxOff eventually becomes nearly rainless and slowly weakens.

Based on the metrics shown in Fig. 5, the vortices in FluxOn and FluxOff behave quite similarly during the first three days; growth is driven primarily by a combination of barotropic instability and coupling with moist convection, which is driven by MSE advection. The same behavior was noted in DB2021, and the importance of MSE advection was highlighted by several recent studies (Adames and Ming 2018b,a; Clark et al. 2020). During this development phase, surface heat fluxes merely act to augment the growth slightly. However, the growth mechanism in the second half of the simulation is quite different. Horizontal MSE advection is not maintaining convection, and energy extracted from the meridional shear is comparatively small. In the next section, we will explore the dynamics of this second growth phase.

### c. The Flux-Dominated Regime

To illustrate the mechanics of vortex growth and coupling with moist convection during the latter half of the simulation, we examine a few relevant meteorological fields for FluxOn and FluxOff for the same set of parameters as in Sec. 4b. Figures 6a,b show the total pressure and total wind at 1.5 km altitude and hourly rain rate at hour 117 for FluxOff and FluxOn, respectively. Figures 6c,d show  $q'_v$  and winds at 0.6 km altitude along with perturbation vertical velocity from the quasi-geostrophic omega equation ( $w_{qg}'$ ), which is calculated using the same procedure as in Diaz and Boos (2019b). As shown in many previous studies (e.g. Rao and Rajamani 1970; Boos et al. 2015; Diaz and Boos 2019b), regions of ascent diagnosed by the quasi-geostrophic omega equation correspond well with precipitation in monsoon depressions.

Two striking features present in the moisture fields of both FluxOn and FluxOff are the wedge of high  $q'_v$  feeding into the region of precipitation and the long ribbon of negative  $q'_v$  to the north (Figs. 6c,d). Both of these features are related to the previously discussed MSE advection, with positive  $q'_v$  from southward vortex winds advecting the basic-state poleward MSE gradient (e.g. Adames and Ming 2018a), and negative  $q'_v$  from the combined westward basic-state and vortex winds advecting negative MSE anomalies that were created from negative advection of meridional basic-state MSE. Otherwise, the two experiments are quite different. Whereas the central region of the vortex in FluxOff has near zero to negative  $q'_v$ , this region in FluxOn has become filled with substantial positive  $q'_v$ . This additional  $q'_v$  comes from surface moisture fluxes and is distinguishable from the  $q'_v$  attributable to advection by its much splotchier appearance. Similar to many observed monsoon depressions, positive  $w'_{qg}$  is located downshear of the circulation center (Fig. 6d). It is colocated with a large part of the region of positive  $q'_v$  attributable to surface moisture fluxes. This colocation likely explains the rainfall distribution, with the highest rain rates located in the southwest

quadrant (Figs. 6b). By contrast, the positive  $w'_{qg}$  in the FluxOff experiment is much weaker and colocated with negative  $q'_v$  (Figs. 6c). This arrangement leads to much lower precipitation rates in FluxOff (Figs. 6a). With much more vigorous convection, the FluxOn experiment has a minimum surface pressure of 985.7 hPa whereas the FluxOff has a pressure of only 997.2 hPa

We next examine the perturbation surface heat flux field corresponding to Fig. 6d (Fig. 7). As the sensible component of the heat flux contributes negligibly to the total, we show only the latent component. For reference, a smoothed outline of the precipitation field is shown, along with near-surface wind vectors. The strongest fluxes are located south of the circulation center. In this region, the strong basic state westerly flow adds to the perturbation westerly flow, leading to a stronger total wind and thus an enhanced flux. Additional enhancements to the flux are brought about by convection, whose downdrafts lead to stronger wind gusts and mix downward air of lower mixing ratio, thus increasing the air-sea disequilibrium. To the north, the fluxes are weaker, because the basic state easterly flow is weaker (Fig. 6b) and there is no moist convection. This pattern of asymmetry about the circulation center roughly matches that of the ERA5 composite, especially when taking into consideration the difference in land cover (Fig. 1a). However, the magnitudes in the simulation are much larger, with a sizable area of  $200 \text{ W m}^{-2}$  to  $300 \text{ W m}^{-2}$  and maximum values just over  $500 \text{ W m}^{-2}$ , compared to a maximum value of just over  $125 \text{ W m}^{-2}$  for the composite. There are a few reasons to suspect that our simulation should have higher fluxes than the composite. Firstly, our simulation is of much higher resolution and therefore better resolves the increase in surface heat flux that is attributable to convective downdrafts. Secondly, whereas the composite is averaged over storms of many different strengths, our simulation represents a strong monsoon depression. Lastly, compositing in general should lead to smoothed fields. For another comparison, the simulation of Fujinami et al. (2020) resulted in surface fluxes exceeding  $300 \text{ W m}^{-2}$  over a sizable area (their figure 9c), which is more in line with our results. However,

one should be cautious with such a comparison, since their figure shows total flux whereas ours shows only perturbation flux.

The above analysis suggests that, during the latter portion of the simulation, the vortex in the FluxOn experiment behaves very differently than it does during the earlier portion. In the latter portion, neither horizontal MSE advection nor dry dynamical processes are substantially helping to intensify the vortex. Instead, the main driver of convection and thus vortex amplification is surface heat fluxes. The interaction of the background flow with the vortex leads to QG forcing for ascent on the downshear side of the vortex. This ascent maintains convection to the southwest of the vortex center, even though the enhanced humidity due to surface fluxes is spread over a broader area. Interestingly, both this mechanism and the MSE advection process lead to roughly similar distributions of rainfall. This similarity results from the fact that warm advection-induced ascent, positive moisture advection, and the total QG ascent all tend to be colocated.

#### *d. Parameter Space Sensitivity*

With a basic understanding of the physical processes governing vortex growth, we now investigate how the parameters  $S_L$ ,  $S_U$ , and  $\zeta_0$  affect vortex intensity and modulate the impact of surface heat fluxes. We use the same parameter combinations as in DB2021, chosen both to represent realistic environments over the Bay of Bengal and to allow a wide range of vortex behaviors.

#### 1) EFFECT OF $S_L$ AND $S_U$ ON STRUCTURE AND INTENSITY

We first look at how  $S_L$  and  $S_U$  impact the intensity and rainfall of the vortex. Since the behavior of the vortex differs substantially between the first and second half of the simulation (see Sec. 4b), we focus our analysis on the second half, the period during which surface fluxes are most important. Figure 8 summarizes all experiments with  $\zeta_0 = 1.0$  as  $S_L$  and  $S_U$  vary. Figure 8a

shows the minimum pressure reached during the final three days of the FluxOn simulation and Fig. 8c shows the total accumulated rainfall over this same time period. These values are calculated following the procedure outlined in Sec. 4b, including averaging the two vortices. To quantify the impact of surface heat fluxes, Fig. 8b shows the difference in minimum pressure between FluxOn and FluxOff and Fig. 8d shows the same quantity as in Fig. 8c, except for the FluxOff simulations.

One of the clearest trends is a reduction in vortex intensity and rainfall with increasing  $|S_U|$  (Fig. 8a, Fig. 8c). For  $S_U = 0$ , some of the vortices reach intensities characteristic of strong tropical cyclones, with sea-level pressure as low as 958.5 hPa. In fact, the vortex at  $S_L = -1.25$ ,  $S_U = 0$  exhibits an eye-like feature toward the end of the simulation (not shown). The effect of  $S_U$  is thus consistent with the consensus that strong wind shear suppresses the growth of tropical cyclones. A similar pattern is noted in the difference plot of pressure (Fig. 8b); although all simulations become stronger when surface fluxes are added, those with lower values of  $|S_U|$  are much more strongly amplified. By contrast, those in the upper right corner are hardly affected by surface fluxes.

The impact of  $S_L$  is more nuanced; the strongest vortices are located along the  $S_L = -1.0$  and  $S_L = -1.25$  rows (Fig. 8a). This outcome is perhaps surprising, since one might expect the parameter space with the weakest vertical shear to have the strongest vortices, because these conditions would be most favorable for tropical cyclones. However, one should keep in mind that these simulations are initialized with a normal mode having a wavelength of 2588 km, rather than from a small-scale vortex as is done in most idealized tropical cyclone modeling studies. This larger size should make it more difficult for tropical cyclones to form. Additionally, some studies argue that weak vertical shear is more favorable for tropical cyclogenesis than no shear at all. For example, Nolan and McGauley (2012) find that 850 hPa to 200 hPa vertical shear values in the range of  $1.25 \text{ m s}^{-1}$  to  $5.0 \text{ m s}^{-1}$  are most favorable for tropical cyclogenesis. For comparison, the 850 hPa to 200 hPa vertical shear for our experiment with  $S_L = -1.25$  and  $S_U = 0.0$  is  $1.4 \text{ m s}^{-1}$  north of the

monsoon trough and  $13.4 \text{ m s}^{-1}$  south of the monsoon trough. Considering that the vortex forms slightly north of the monsoon trough axis, it is probably exposed to vertical shear magnitudes near or within the favorable range discussed by Nolan and McGauley (2012). Nevertheless, within the context of our experiments, this comparison with tropical cyclones does not provide a physical explanation of why higher values of  $|S_L|$  have stronger vortices.

A starting point for explaining the  $S_L$  pattern comes from comparing Fig. 8c and Fig. 8d: the FluxOn experiments that produce the most rain are located in the same region of parameter space as the FluxOff experiments that produce the most rain. The rainfall trends in FluxOff likely result from the MSE advection process discussed in Sec. 4b, with rainfall increasing with the steepening meridional moisture gradient that accompanies increases in  $|S_L|$ . However, given the much smaller rainfall totals in FluxOff (note the change in color scales between Fig. 8c and Fig. 8d), this process alone is insufficient to explain why rainfall increases with  $|S_L|$  in FluxOn. A more plausible explanation comes from comparing time series of pressure, rain, and MSE for the  $S_L = 0$  and  $S_L = -1.0$  experiments with  $S_U$  fixed at  $-1.0$  (Fig. 9). These quantities are calculated in the same manner as in Sec. 4b. As expected, MSE advection during the first day is substantially lower with  $S_L = 0.0$  than with  $S_L = -1.0$  (Fig. 9b,d). Consequently, the vortex with  $S_L = 0.0$  produces much less rainfall (Fig. 9a,c). However, by the middle of the simulation, MSE advection in the  $S_L = -1.0$  experiment becomes strongly negative, while remaining near zero to slightly positive in the  $S_L = 0.0$  experiment. Thus, one possible explanation for the stronger vortex in the simulation with larger  $|S_L|$  is that the much stronger MSE advection early on gave it a head start over the vortex in the  $S_L = 0.0$  experiment. The convection resulting from this MSE advection moistened the vortex and led to more latent heat release, creating a stronger vortex that was better suited to take advantage of surface heat fluxes as an energy source. In fact, while surface heat fluxes become a

substantial MSE source in the  $S_L = -1.0$  experiment, they contribute little to MSE in the  $S_L = 0.0$  experiment (Fig. 9b,d).

For more insight into how variations in  $S_L$  and  $S_U$  affect the vortices, we examine maps of their rain rate and total pressure at day 4.5 for all experiments with  $\zeta_0 = 1.0$  (Fig. 10). Consistent with Fig. 8a,c, the strongest,雨iest vortices are located in the lower-left corner of Fig. 10. As  $|S_L|$  increases, the precipitation evolves from being more randomly distributed about the center of circulation to being increasingly biased toward the southwest quadrant, an arrangement one would expect in a monsoon depression (c.f. Fig. 1a). This pattern is consistent with vertical wind shear inducing QG forcing for ascent downshear of the vortex, as noted in Sec. 4c.

Also noteworthy is that the vortex tends to be centered near or just north of  $20^\circ N$ , the latitude where the strongest meridional gradients of both meridional and vertical shear are located (Fig. 2a). This position reflects the favorability of the monsoon trough axis for vortex development. A similar arrangement is seen in observed monsoon depressions (Fig. 1a). Consequently, if the vortex is centered just north of the monsoon trough axis, it would be subjected to substantially less vertical shear than if it were centered further south.

## 2) EFFECT OF $\zeta_0$ AND $S_L$ ON STRUCTURE AND INTENSITY

We now compare experiments with different values of  $\zeta_0$ , the parameter that controls the low-level meridional shear. For this set of experiments,  $S_U$  is held constant at  $-2.0$  while  $S_L$  is varied. Figure 11 shows the minimum pressure and total rainfall calculated in the same manner as in Fig. 8. Recall that the pressure and rainfall values are evaluated over the second half of the simulation.

The most distinct trend is the increasing intensity and rainfall with  $\zeta_0$  (Fig. 11a,c). As discussed in DB2021, this intensification trend results primarily from the basic state becoming more barotropically unstable. Comparing the FluxOn and FluxOff simulations, surface fluxes intensify

the vortices more strongly as  $\zeta_0$  increases (Fig. 11b). In fact, when  $\zeta_0 = 0$ , surface fluxes have little to no effect on these two metrics. The explanation is likely similar to that given in Sec. 4d1: in order for surface fluxes to be beneficial, other processes, such as barotropic instability, must bring the vortex to a sufficient intensity. If nothing intensifies the vortex (as in  $\zeta_0 = 0.0$ ), surface fluxes will not lead to any additional amplification.

A secondary pattern among these simulations is the general increase in intensity and rainfall with increasing  $|S_L|$ . As discussed in Sec. 4d1 and detailed in DB2021, this pattern results from MSE advection organizing more convection as  $S_L$  increases. However, the strongest vortices are located on the  $S_L = -1.25$  row rather than on the  $S_L = -1.5$  row (Fig. 11a). We speculate that there is a trade off between MSE advection being favorable for vortex amplification and vertical shear being unfavorable, with  $S_L = -1.25$  representing a compromise between the two. One clear exception to both of these trends is the local maximum in intensity seen at  $\zeta_0 = 0.5$  and  $S_L = 0$ . We find no obvious reason for this exception. Animations reveal that it develops more centralized convection compared to the other simulations, suggesting that it exhibits more tropical cyclone-like properties (not shown).

Snapshots of total pressure and rain rate for this suite of experiments at day 4.5 are shown in Fig. 12. The strengthening trend with increasing  $\zeta_0$  is accompanied by dramatic changes in structure. At  $\zeta_0 = 0$ , there is no rainfall and little evidence of a perturbation. For  $\zeta_0 = 0.5$ , there is a weak trough of lower pressure with rainfall, but few if any closed isobars. As  $\zeta_0$  increases to 1.5, the vortices become especially monsoon depression-like, with most exhibiting intense rainfall south and west of their circulation center but little to no rainfall in other parts of their circulation. This trend demonstrates once again that the low-level meridional shear is crucial to the development of these vortices. Although we attribute this pattern primarily to the environment becoming increasing barotropically unstable, an additional factor that should not be overlooked is the change in vertical

shear that accompanies variations in  $\zeta_0$  (Fig. 2a). Since the vortices are centered north of 20°N, they are subjected to ever lessening vertical shear as  $\zeta_0$  increases. This weaker shear may allow the vortex to remain more vertically aligned, and thus achieve higher intensities. However, as in DB2021, our analysis of the perturbation kinetic energy budget shows that vortex interaction with the basic-state meridional shear does enhance intensity through a process akin to barotropic instability (not shown). By contrast, the evolution in structure as  $|S_L|$  increases is less drastic. For  $S_L = 0$ , the precipitation is weaker and less asymmetric, since the low-level MSE gradient and vertical wind shear are substantially weaker. As  $|S_L|$  goes up, the rainfall field becomes increasingly asymmetric for the stronger vortices at  $\zeta_0 = 1.0$  and  $\zeta_0 = 1.5$ .

## 5. Summary and Discussion

Adding surface heat fluxes to our simulations of vortices in a broad range of background wind shears results in vortices that are substantially stronger. During the initial rapid intensification of these vortices, energy input from surface fluxes augments growth from barotropic instability and from coupling with moist convection induced by MSE advection. However, during the second half of the simulations, the vortices enter a different growth regime; barotropic instability and MSE advection become less important as the main energy source shifts to surface heat fluxes. During this phase, convection is organized by both surface heat fluxes and QG forcing for ascent. In simulations without surface fluxes, this phase does not occur, and the vortex weakens as its rainfall rate declines. Taken in conjunction with the results of DB2021, this study suggests that there are at least three distinct mechanisms by which monsoon depressions can amplify: barotropic instability, convective coupling through MSE advection, and convective coupling through surface fluxes. It is possible that QG ascent provides the lifting needed to trigger consumption of the convective available potential energy that is generated by MSE advection and surface fluxes. In

our simulations, these three processes seem to happen independently. It is unclear whether this is representative of observed monsoon depressions or whether it is an artifact of our experimental design.

The impact of surface heat fluxes is strongly dependent upon the basic state shear. As upper-level shear increases, the contribution that surface fluxes make to the vortex intensity diminishes. This behavior is reminiscent of tropical cyclones, which tend to weaken as wind shear becomes large. In fact, when our upper-level shear parameter is set to zero, some of the vortices become tropical cyclones. However, contrary to this notion, increasing low-level shear actually leads to stronger vortices, at least below a certain threshold. As in DB2021, we attribute this tendency to the MSE gradient steepening as the magnitude of low-level shear increases. The associated strengthening of meridional MSE advection allows for more convective coupling early in the vortex's life cycle, and thus more intensification. The resulting stronger vortex is then better able to take advantage of surface fluxes for growth, since their contribution to moistening is a strong function of the perturbation wind near the surface. Thus, meridional MSE advection seems to influence vortex evolution even after it ceases to be an important MSE source. For higher magnitudes of lower-level shear, intensity falls off once again. We speculate that there is a trade off between the detrimental effect of vertical wind shear and the beneficial effect of a stronger MSE gradient.

However, exerting even more control on vortex intensity than the MSE gradient is the magnitude of the lower-level meridional shear. Without this shear, very little growth occurs, even in the presence of surface fluxes. We attribute most of this trend to the environment becoming more barotropically unstable, because our PKE budgets indicate that barotropic energy conversion increases monotonically with the strength of the meridional shear (not shown). Nevertheless, it is possible that weakening vertical shear north of the monsoon trough axis that accompanies the increase in meridional shear could also be a contributing factor.

Our results generally corroborate those of earlier studies of monsoon depressions, though with a few minor discrepancies. Consistent with the case study of Fujinami et al. (2020), including surface fluxes results in a stronger vortex. However, unlike their study, the vortices in our experiments still undergo a period a rapid strengthening in the absence of surface fluxes. This difference could partly result from the experimental design. Whereas we exclude only the perturbation flux, Fujinami et al. (2020) excludes the total flux. This could predispose their experiments to produce larger differences in intensity and rainfall. Our results are also partially consistent with those of Diaz and Boos (2019b), who performed a similar type of surface flux denial experiment as in the present study, but using a more complicated basic state constructed from a reanalysis data set. Although they also found that surface fluxes enhanced vortex growth, the present study suggests a comparatively larger role for surface fluxes. This difference is probably attributable to the presence of land in the experiments of Diaz and Boos (2019b), over which the anomalous flux was set to zero. The simulated monsoon depression in Diaz and Boos (2019b) made landfall soon after it formed, thus limiting the potential for growth from surface fluxes. Therefore, it is possible that, for a similar set of shear parameters, the vortices in our experiments reach higher intensities than typical observed monsoon depressions, which usually make landfall within a few days of forming. Our idealized simulations might also better represent storms that form over the central or eastern Bay of Bengal and thus take longer to make landfall. Additionally, the growth regime in which the vortex is drawing energy primarily from surface fluxes is similar to that explored by Murthy and Boos (2020) using a column QG model. They find that QG ascent contributes about 40% to the rainfall, surface fluxes an additional 40%, and moisture advection another 20%. They note however, that most of the QG ascent results from diabatic heating, whereas we calculated only the dry component. Although our results would seem to contradict Adames and Ming (2018b), who find little enhancement from surface fluxes, we find multiple growth mechanisms to be

important and it is possible that the vortices they simulate are governed more by MSE advection or barotropic growth than they are in our simulations. Furthermore, since their analysis relies on linear regressions that are filtered in time and space to make a composite disturbance, it is possible that their analysis technique emphasizes one mechanism over the other.

*Acknowledgments.* This material is based upon work supported by the U.S. Department of Energy (DOE), Office of Science, Office of Biological and Environmental Research, Climate and Environmental Sciences Division, Regional and Global Model Analysis Program, under Award DE-SC0019367. It used resources of the National Energy Research Scientific Computing Center (NERSC), which is a DOE Office of Science User Facility.

*Data availability statement.* The numerical model simulations upon which this study is based are too large to archive or to transfer. However, the model source code, along with instructions on how to compile and run it, are provided at <https://github.com/michaeldiaz0/Model1>.

## References

- Adames, Á. F., and Y. Ming, 2018a: Interactions between water vapor and potential vorticity in synoptic-scale monsoonal disturbances: Moisture vortex instability. *Journal of the Atmospheric Sciences*, **75** (6), 2083–2105.
- Adames, Á. F., and Y. Ming, 2018b: Moisture and moist static energy budgets of South Asian monsoon low pressure systems in GFDL AM4.0. *Journal of the Atmospheric Sciences*, **75** (6), 2107–2123.
- Boos, W., J. Hurley, and V. Murthy, 2015: Adiabatic westward drift of Indian monsoon depressions. *Quarterly Journal of the Royal Meteorological Society*, **141** (689), 1035–1048.

Clark, S. K., Y. Ming, and Á. F. Adames, 2020: Monsoon low pressure system–like variability in an idealized moist model. *Journal of Climate*, **33** (6), 2051–2074.

Diaz, M., and W. R. Boos, 2019a: Barotropic growth of monsoon depressions. *Quarterly Journal of the Royal Meteorological Society*, **145** (719), 824–844.

Diaz, M., and W. R. Boos, 2019b: Monsoon depression amplification by moist barotropic instability in a vertically sheared environment. *Quarterly Journal of the Royal Meteorological Society*, **145** (723), 2666–2684.

Diaz, M., and W. R. Boos, 2021: Evolution of idealized vortices in monsoon-like shears: application to monsoon depressions. *Journal of the Atmospheric Sciences*, **78** (4), 1207–1225.

Emanuel, K. A., and R. Rotunno, 1989: Polar lows as arctic hurricanes. *Tellus A: Dynamic Meteorology and Oceanography*, **41** (1), 1–17.

Fujinami, H., H. Hirata, M. Kato, and K. Tsuboki, 2020: Mesoscale precipitation systems and their role in the rapid development of a monsoon depression over the bay of bengal. *Quarterly Journal of the Royal Meteorological Society*, **146** (726), 267–283.

Hersbach, H., and Coauthors, 2020: The era5 global reanalysis. *Quarterly Journal of the Royal Meteorological Society*.

Hunt, K. M., and A. G. Turner, 2017: The effect of soil moisture perturbations on indian monsoon depressions in a numerical weather prediction model. *Journal of Climate*, **30** (21), 8811–8823.

Hunt, K. M., A. G. Turner, P. M. Inness, D. E. Parker, and R. C. Levine, 2016: On the structure and dynamics of Indian monsoon depressions. *Monthly Weather Review*, **144** (9), 3391–3416.

Kishtawal, C., D. Niyogi, B. Rajagopalan, M. Rajeevan, N. Jaiswal, and U. Mohanty, 2013: Enhancement of inland penetration of monsoon depressions in the bay of bengal due to prestorm ground wetness. *Water resources research*, **49** (6), 3589–3600.

Murthy, V. S., and W. R. Boos, 2020: Quasigeostrophic controls on precipitating ascent in monsoon depressions. *Journal of the Atmospheric Sciences*, **77** (4), 1213–1232.

Nolan, D. S., and M. G. McGauley, 2012: Tropical cyclogenesis in wind shear: Climatological relationships and physical processes. Nova Science Publishers Happlege, New York, 1–36 pp.

Rao, K., and S. Rajamani, 1970: Diagnostic study of a monsoon depression by geostrophic baroclinic model. *Indian Journal of Meteorology and Geophysics*, **21**, 187–194.

Rotunno, R., and K. A. Emanuel, 1987: An air–sea interaction theory for tropical cyclones. part ii: Evolutionary study using a nonhydrostatic axisymmetric numerical model. *Journal of the Atmospheric Sciences*, **44** (3), 542–561.

Thangaprakash, V., and Coauthors, 2016: What controls seasonal evolution of sea surface temperature in the bay of bengal? mixed layer heat budget analysis using moored buoy observations along 90 e. *Oceanography*, **29** (2), 202–213.

Tippett, M. K., S. J. Camargo, and A. H. Sobel, 2011: A poisson regression index for tropical cyclone genesis and the role of large-scale vorticity in genesis. *Journal of Climate*, **24** (9), 2335–2357.

Uccellini, L. W., 1990: Processes contributing to the rapid development of extratropical cyclones. *Extratropical cyclones*, Springer, 81–105.

## LIST OF FIGURES

- Fig. 1.** Composite monsoon depression from ERA5 reanalysis based on the 1982-2018 IMD track dataset. (a) shows anomalous surface precipitation rate (shading,  $\text{mm h}^{-1}$ ), 850 hPa to 200 hPa vertical shear of the zonal wind (contours,  $\text{m s}^{-1}$ ), and anomalous 10 m wind (vectors). (b) shows anomalous surface latent heat flux (shading,  $\text{W m}^{-2}$ ), anomalous surface sensible heat flux (contoured every  $10 \text{ W m}^{-2}$ , excluding zero), and anomalous 10 m wind (vectors). All anomalies are from the time-mean climatology. . . . .

**Fig. 2.** Basic state vertical wind shear for various combinations of  $\zeta_0$ ,  $S_L$ , and  $S_U$ . (a) shows 850 hPa to 200 hPa basic state zonal wind shear ( $\Delta\bar{U}$ ,  $\text{m s}^{-1}$ ) as a function of latitude. (b) and (c) show basic state vertical shear of the zonal wind ( $\partial_z\bar{U}$ ,  $\text{m s}^{-1} \text{ km}^{-1}$ ) as a function of height. The thick lines show profiles south of the monsoon trough axis (which lies at  $20^\circ\text{N}$ ) and the thin lines show profiles north of this axis, both within the regions where vertical shear is constant with latitude, as shown in (a). . . . .

**Fig. 3.** Profiles of vertical shear of the zonal wind for a pre-genesis composite of monsoon depression environments compared with those shown in Fig. 2. (a) shows the same as in Fig. 2a, but for the composite profile (red line). The gray shading indicates the ranges of values shown in Fig. 2a, but shifted to be centered at  $21^\circ\text{N}$ . (b) and (c) show basic state vertical shear of the zonal wind ( $\partial_z\bar{U}$ ) as a function of height for the composite profile (red line). The gray shading indicates the ranges of values shown in Fig. 2b,c. Thick solid lines show actual wind shear and thin dashed lines wind shear calculated from thermal wind balance. The red lines in (b) are a  $21^\circ\text{N}$ - $25^\circ\text{N}$  average at  $90^\circ\text{E}$  and the red lines in (c) are a  $17^\circ\text{N}$ - $21^\circ\text{N}$  average at  $90^\circ\text{E}$ . . . . .

**Fig. 4.** Sample monsoon depression from  $\zeta_0 = 1.5$ ,  $S_L = -1.0$ , and  $S_U = -2.0$  at hour 78. (a) shows perturbation potential temperature (shading,  $\theta'$ , K), total pressure (contoured by 0.75 hPa with a minimum contour of 395.25 hPa), and wind vectors at 7.6 km. (b) shows the vertically integrated condensate from the surface to 15 km (shading,  $q_c + q_i + q_s + q_r$ ,  $\text{g kg}^{-1}$ ), total pressure (contoured by 2.0 hPa with a minimum contour of 699.0 hPa), and wind vectors at 3.0 km, (c) is the same as (a) expect at 0.6 km with pressure contoured by 2.0 hPa with a minimum contour of 928.0 hPa. The background map is for scale reference only and has no effect on the simulations. . . . .

**Fig. 5.** Time series of various metrics over the life cycle of the vortex for  $\zeta_0 = 1.0$ ,  $S_L = -1.25$ , and  $S_U = -1.0$ . (a) shows minimum perturbation pressure at 1.5 km (black, hPa) and rain rate (green,  $\text{mm h}^{-1}$ ). The solid lines are for FluxOn, the dashed lines for FluxOff, and the dotted lines for Dry. (b) shows select terms in the vertically integrated MSE budget. Solid lines are for FluxOn and dashed lines are for FluxOff. The black lines show total perturbation MSE ( $1000 \text{ J kg}^{-1}$ ), the red line shows total horizontal MSE advection ( $1000 \text{ J kg}^{-1}$ , first two terms on the right-hand side of Eq. 6), and the green line shows MSE from surface heat fluxes (last term on right-hand side of Eq. 6). (c) shows the meridional shear term ( $u'v'd_y\bar{U}$ ) in the PKE equation. The solid line shows FluxOn, the dashed line shows FluxOff, and the dotted line shows Dry. (d) shows the same as (c), but for the pressure work term. . . . .

**Fig. 6.** Comparison between FluxOff (a,c) and FluxOn (b,d) for  $\zeta_0 = 1.0$ ,  $S_L = -1.25$ , and  $S_U = -1.0$  at hour 117. (a) and (b) show hourly rain rates over the previous three hours (shading,  $\text{mm h}^{-1}$ ), total pressure at 1.5 km (contoured by 1.5 hPa with 842 hPa contour labeled), and total wind (vectors,  $\mathbf{v}$ , 1.5 km). (c) and (d) show perturbation mixing ratio (shading,  $q_v$ ,  $\text{g kg}^{-1}$ , 0.6 km), perturbation vertical velocity from the QG-omega equation (contoured on log-2 scale beginning at  $0.5 \text{ cm s}^{-1}$  and smoothed with a Gaussian filter, with upward motion in solid contours), and total wind (vectors,  $\mathbf{v}$ , 0.6 km). . . . .

<b>Fig. 7.</b> Perturbation surface latent heat fluxes (shading, $\text{W m}^{-2}$ ), total rain rate (smoothed 5 $\text{mm h}^{-1}$ contour), and perturbation near-surface winds (vectors) for the same experiment as shown in Fig. 6 at hour 117. . . . .	38
<b>Fig. 8.</b> Summary statistics for experiments with $\zeta_0 = 1.0$ for various values of $S_L$ and $S_U$ . (a) shows the minimum pressure reached for the second half of the FluxOn simulation (hPa). Pressure is given as both the perturbation value at 1.5 km (upper number) and the total value at the surface (lower number), expressed without the first digit (e.g. 983.7 hPa = 83.7). (b) shows the difference between FluxOn and FluxOff for the perturbation pressure shown in (a). (c) shows the three-day accumulated rainfall for the second half of the FluxOn experiment (mm). Each value is the average within a $10^\circ \times 10^\circ$ box centered on the minimum perturbation pressure at 1.5 km. (d) shows the same as (c), except for FluxOff. All values are the average of the two vortices. Note the difference in color scales between (a) and (b) and between (c) and (d). . . . .	39
<b>Fig. 9.</b> Time series comparison of pressure, rain, and MSE for two experiments. (a) and (b) are the same as Fig. 5a and Fig. 5b, but for $\zeta_0 = 1.0$ , $S_L = 0.0$ , and $S_U = -1.0$ . (c) and (d) are the same as (a) and (b), but for $S_L = -1.0$ . . . . .	40
<b>Fig. 10.</b> Rain rate (shading, $\text{mm h}^{-1}$ ) and total pressure (contoured every 1.5 hPa ) for all experiments with $\zeta_0 = 1.0$ for various values of $S_L$ and $S_U$ at day 4.5 of the simulation. The 842 hPa isobar is dashed for ease of comparison. . . . .	41
<b>Fig. 11.</b> Same as Fig. 8, but for variations in $\zeta_0$ and $S_L$ . . . . .	42
<b>Fig. 12.</b> Same as Fig. 10, but for variations in $\zeta_0$ and $S_L$ . . . . .	43

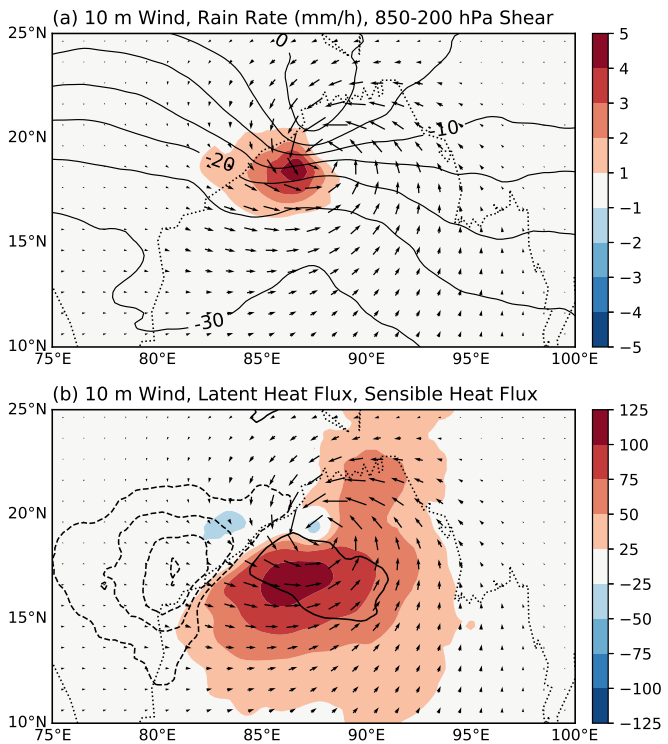


FIG. 1. Composite monsoon depression from ERA5 reanalysis based on the 1982–2018 IMD track dataset. (a) shows anomalous surface precipitation rate (shading,  $\text{mm h}^{-1}$ ), 850 hPa to 200 hPa vertical shear of the zonal wind (contours,  $\text{ms}^{-1}$ ), and anomalous 10 m wind (vectors). (b) shows anomalous surface latent heat flux (shading,  $\text{W m}^{-2}$ ), anomalous surface sensible heat flux (contoured every  $10 \text{ W m}^{-2}$ , excluding zero), and anomalous 10 m wind (vectors). All anomalies are from the time-mean climatology.

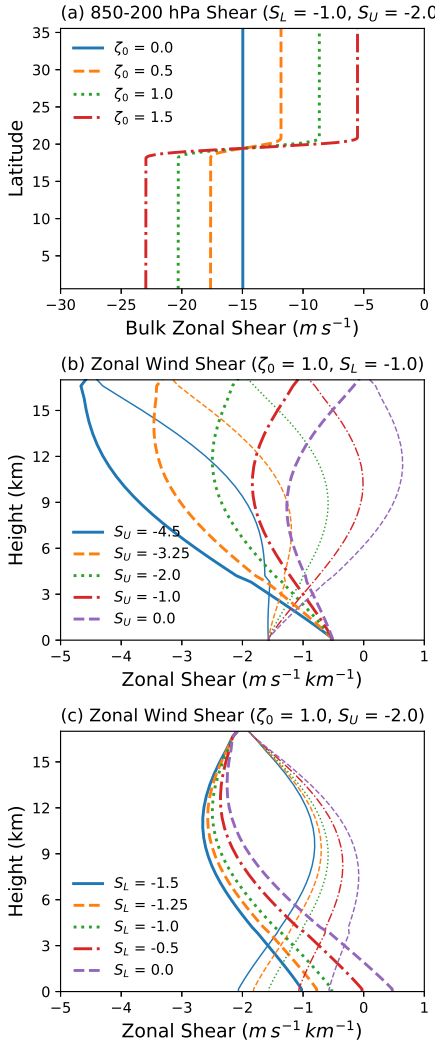


FIG. 2. Basic state vertical wind shear for various combinations of  $\zeta_0$ ,  $S_L$ , and  $S_U$ . (a) shows 850 hPa to 200 hPa basic state zonal wind shear ( $\Delta\bar{U}$ ,  $m s^{-1}$ ) as a function of latitude. (b) and (c) show basic state vertical shear of the zonal wind ( $\partial_z\bar{U}$ ,  $m s^{-1} km^{-1}$ ) as a function of height. The thick lines show profiles south of the monsoon trough axis (which lies at  $20^{\circ}N$ ) and the thin lines show profiles north of this axis, both within the regions where vertical shear is constant with latitude, as shown in (a).

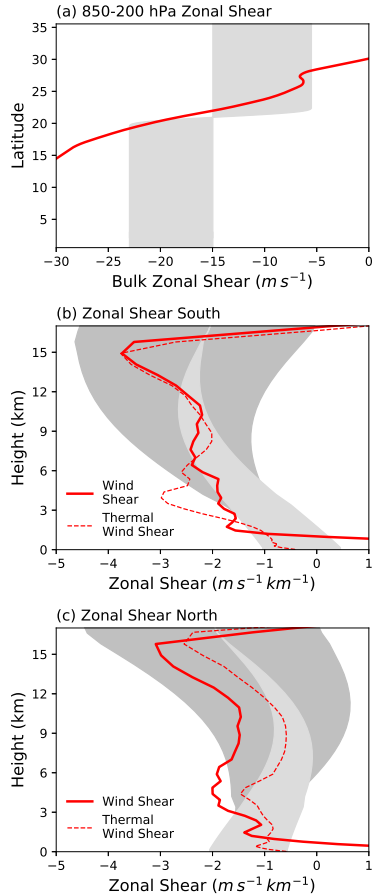


FIG. 3. Profiles of vertical shear of the zonal wind for a pre-genesis composite of monsoon depression environments compared with those shown in Fig. 2. (a) shows the same as in Fig. 2a, but for the composite profile (red line). The gray shading indicates the ranges of values shown in Fig. 2a, but shifted to be centered at 21°N. (b) and (c) show basic state vertical shear of the zonal wind ( $\partial_z \bar{U}$ ) as a function of height for the composite profile (red line). The gray shading indicates the ranges of values shown in Fig. 2b,c. Thick solid lines show actual wind shear and thin dashed lines wind shear calculated from thermal wind balance. The red lines in (b) are a 21°N-25°N average at 90°E and the red lines in (c) are a 17°N-21°N average at 90°E.

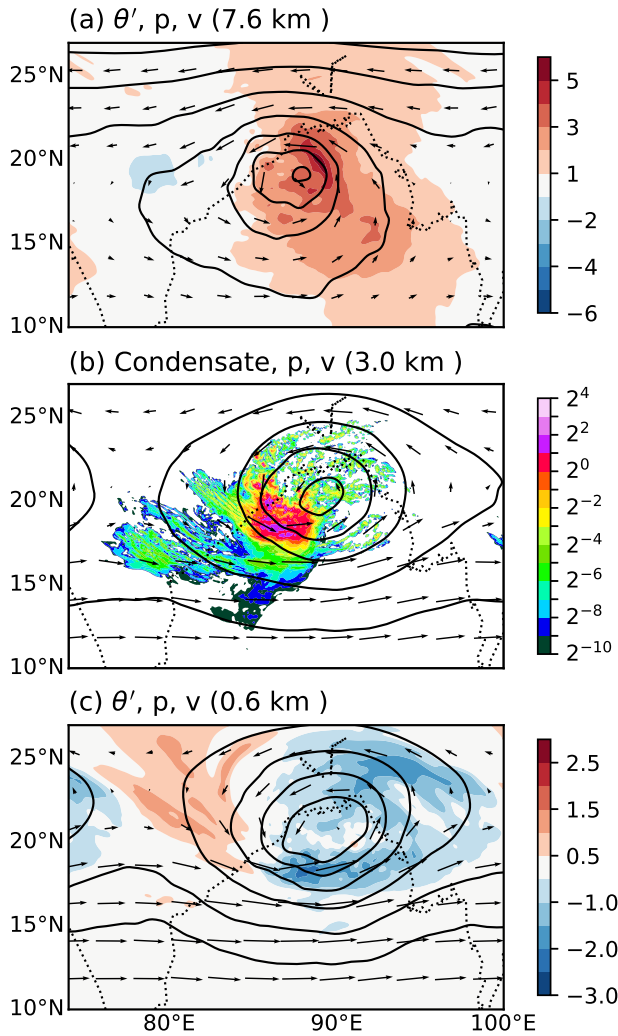


FIG. 4. Sample monsoon depression from  $\zeta_0 = 1.5$ ,  $S_L = -1.0$ , and  $S_U = -2.0$  at hour 78. (a) shows perturbation potential temperature (shading,  $\theta'$ , K), total pressure (contoured by 0.75 hPa with a minimum contour of 395.25 hPa), and wind vectors at 7.6 km. (b) shows the vertically integrated condensate from the surface to 15 km (shading,  $q_c + q_i + q_s + q_r$ ,  $\text{g kg}^{-1}$ ), total pressure (contoured by 2.0 hPa with a minimum contour of 699.0 hPa), and wind vectors at 3.0 km, (c) is the same as (a) expect at 0.6 km with pressure contoured by 2.0 hPa with a minimum contour of 928.0 hPa. The background map is for scale reference only and has no effect on the simulations.

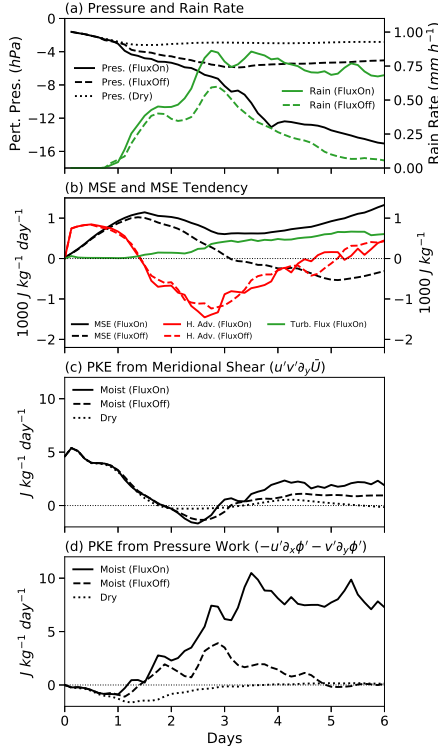


FIG. 5. Time series of various metrics over the life cycle of the vortex for  $\zeta_0 = 1.0$ ,  $S_L = -1.25$ , and  $S_U = -1.0$ .

(a) shows minimum perturbation pressure at 1.5 km (black, hPa) and rain rate (green, mmh<sup>-1</sup>). The solid lines are for FluxOn, the dashed lines for FluxOff, and the dotted lines for Dry. (b) shows select terms in the vertically integrated MSE budget. Solid lines are for FluxOn and dashed lines are for FluxOff. The black lines show total perturbation MSE (1000 J kg<sup>-1</sup>), the red line shows total horizontal MSE advection (1000 J kg<sup>-1</sup>, first two terms on the right-hand side of Eq. 6), and the green line shows MSE from surface heat fluxes (last term on right-hand side of Eq. 6). (c) shows the meridional shear term ( $u'v'\partial_y\bar{U}$ ) in the PKE equation. The solid line shows FluxOn, the dashed line shows FluxOff, and the dotted line shows Dry. (d) shows the same as (c), but for the pressure work term.

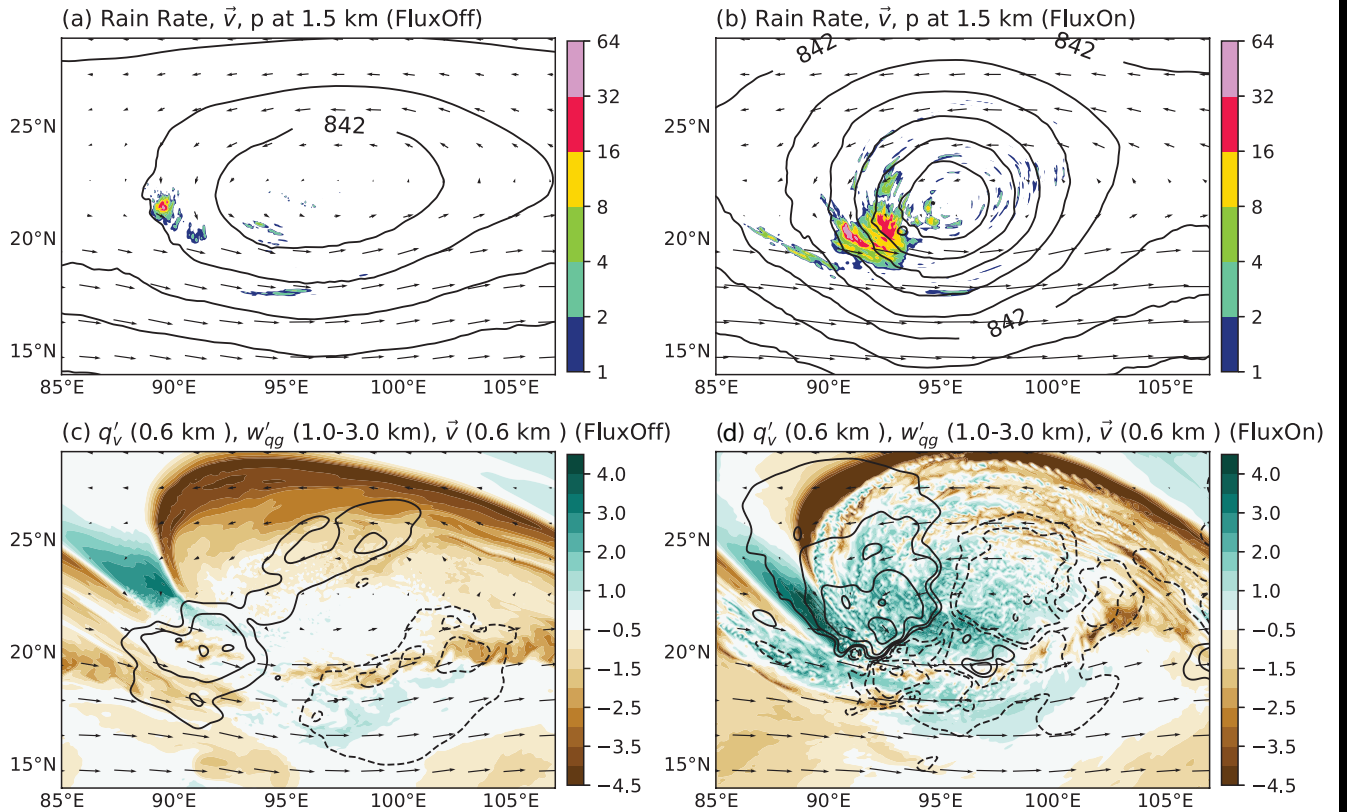


FIG. 6. Comparison between FluxOff (a,c) and FluxOn (b,d) for  $\zeta_0 = 1.0$ ,  $S_L = -1.25$ , and  $S_U = -1.0$  at hour 117. (a) and (b) show hourly rain rates over the previous three hours (shading,  $\text{mm h}^{-1}$ ), total pressure at 1.5 km (contoured by 1.5 hPa with 842 hPa contour labeled), and total wind (vectors,  $\mathbf{v}$ , 1.5 km). (c) and (d) show perturbation mixing ratio (shading,  $q_v'$ ,  $\text{g kg}^{-1}$ , 0.6 km), perturbation vertical velocity from the QG-omega equation (contoured on log-2 scale beginning at  $0.5 \text{ cm s}^{-1}$  and smoothed with a Gaussian filter, with upward motion in solid contours), and total wind (vectors,  $\mathbf{v}$ , 0.6 km).

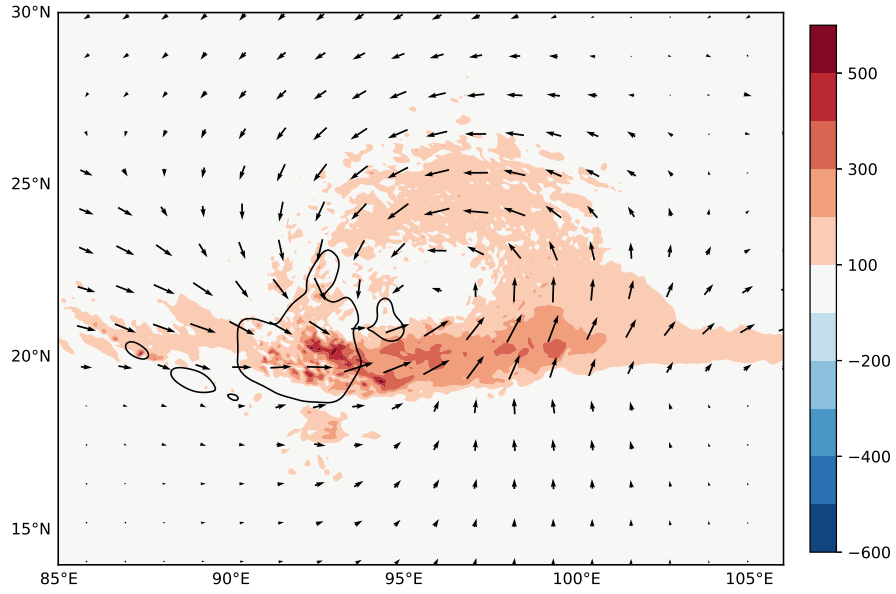


FIG. 7. Perturbation surface latent heat fluxes (shading,  $\text{W m}^{-2}$ ), total rain rate (smoothed  $5 \text{ mm h}^{-1}$  contour), and perturbation near-surface winds (vectors) for the same experiment as shown in Fig. 6 at hour 117.

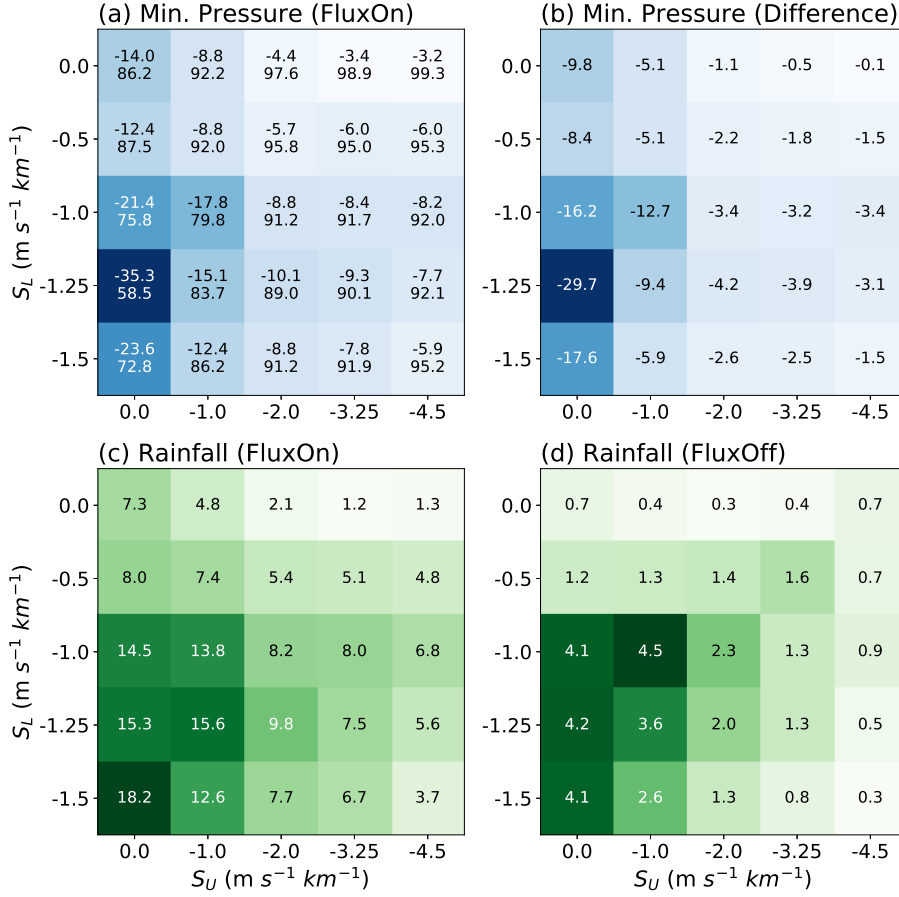


FIG. 8. Summary statistics for experiments with  $\zeta_0 = 1.0$  for various values of  $S_L$  and  $S_U$ . (a) shows the minimum pressure reached for the second half of the FluxOn simulation (hPa). Pressure is given as both the perturbation value at 1.5 km (upper number) and the total value at the surface (lower number), expressed without the first digit (e.g. 983.7 hPa = 83.7). (b) shows the difference between FluxOn and FluxOff for the perturbation pressure shown in (a). (c) shows the three-day accumulated rainfall for the second half of the FluxOn experiment (mm). Each value is the average within a  $10^\circ \times 10^\circ$  box centered on the minimum perturbation pressure at 1.5 km. (d) shows the same as (c), except for FluxOff. All values are the average of the two vortices. Note the difference in color scales between (a) and (b) and between (c) and (d).

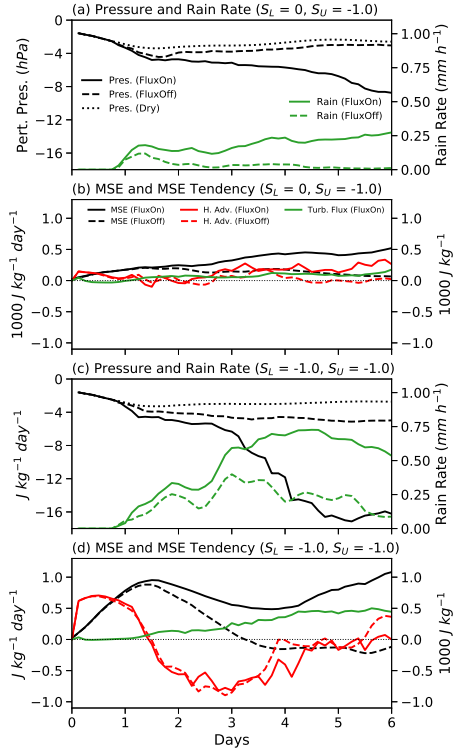


FIG. 9. Time series comparison of pressure, rain, and MSE for two experiments. (a) and (b) are the same as Fig. 5a and Fig. 5b, but for  $\zeta_0 = 1.0$ ,  $S_L = 0.0$ , and  $S_U = -1.0$ . (c) and (d) are the same as (a) and (b), but for  $S_L = -1.0$ .

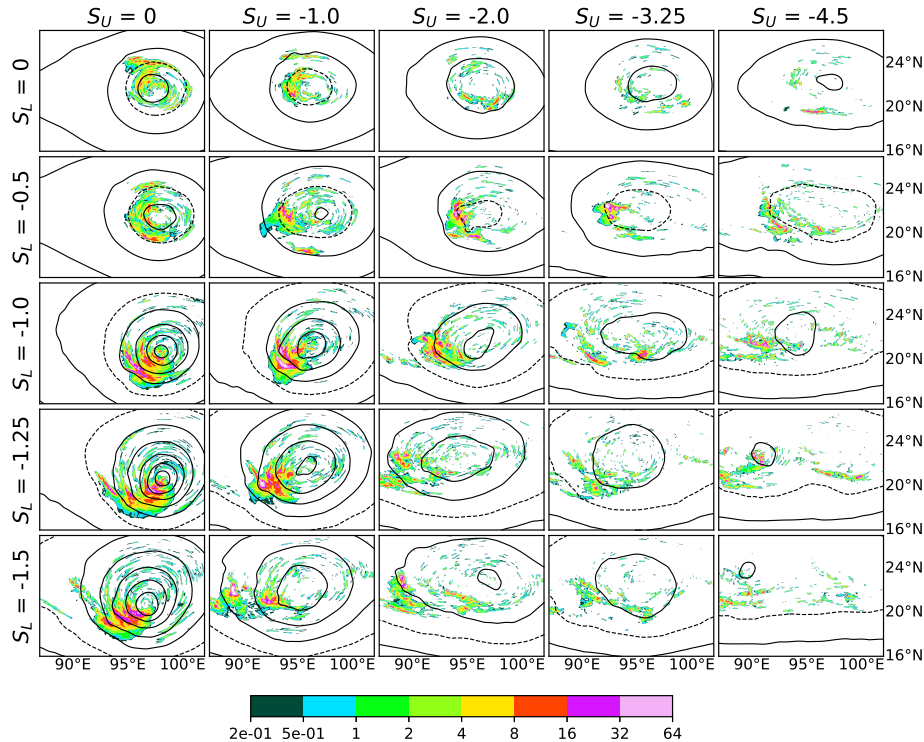


FIG. 10. Rain rate (shading,  $\text{mm h}^{-1}$ ) and total pressure (contoured every 1.5 hPa) for all experiments with  $\zeta_0 = 1.0$  for various values of  $S_L$  and  $S_U$  at day 4.5 of the simulation. The 842 hPa isobar is dashed for ease of comparison.

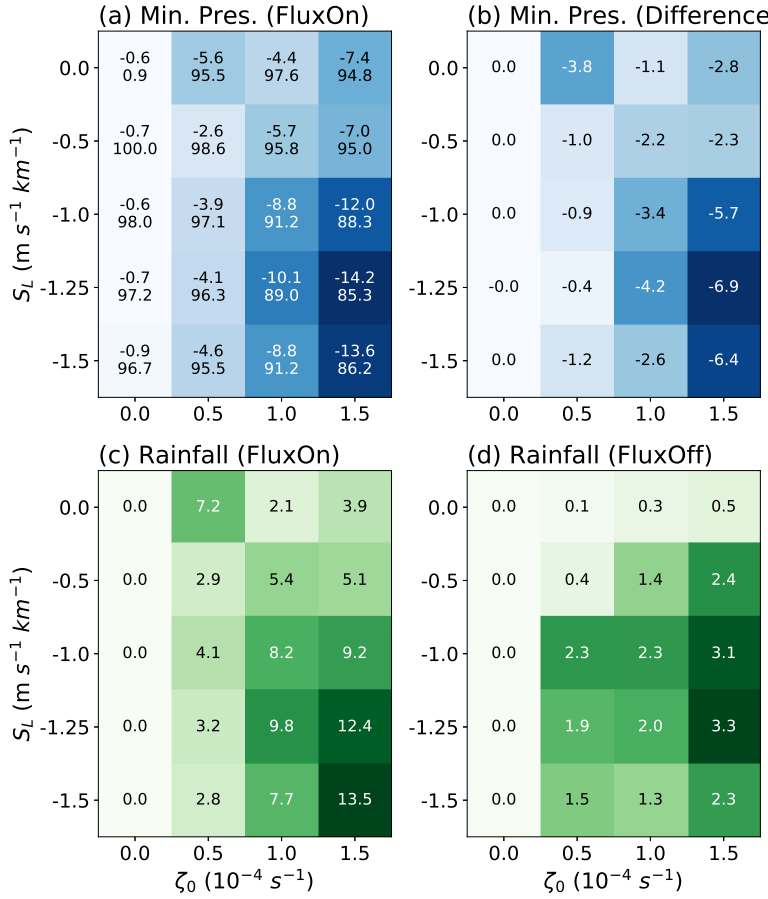


FIG. 11. Same as Fig. 8, but for variations in  $\zeta_0$  and  $S_L$ .

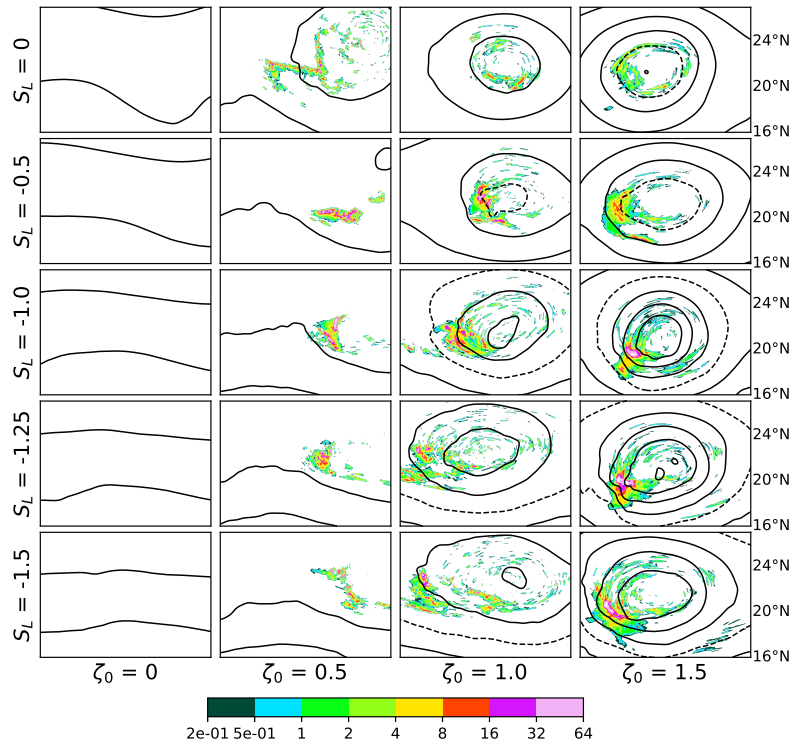


FIG. 12. Same as Fig. 10, but for variations in  $\zeta_0$  and  $S_L$ .